Solar Energy Materials & Solar Cells 290 (2025) 113657

Contents lists available at ScienceDirect

Solar Energy Materials and Solar Cells

journal homepage: www.elsevier.com/locate/solmat

Computational simulation of perovskite and silicon solar panel operating temperatures in varying ambient conditions

Julianna Varjopuro [a], Aleksi Kamppinen [a,*], Aapo Poskela [a], Juha A. Karhu [b], Anders V. Lindfors [b], Kati Miettunen [a]

[a] Department of Mechanical and Materials Engineering, University of Turku, Vesilinnantie 5, Turku, 20500, Finland
[b] Finnish Meteorological Institute, Erik Palmenin aukio 1, Helsinki, 00560, Finland

ARTICLE INFO

Dataset link: https://doi.org/10.57707/fmi-b2share.fbe73c1d7c144ce787db3785302dd1e1, https://github.com/juliavarjop/Comparison_of_PVK_and_Si_panel_temperatures

Keywords:
Photovoltaic
Perovskite
Thermal model
Module temperature
Temperature prediction
Weather condition

ABSTRACT

In this study, the thermal behavior of perovskite panels is modeled in different ambient conditions, and simulated operation temperatures are compared with those of more commonly studied silicon solar panels. One specific need is for temperature model parameters for perovskite panels, to make, for instance, photovoltaic power prediction models that are more consistent with those of silicon solar panels. While the operating temperature of perovskite panels has gained less attention, it impacts their stability more compared with silicon devices. The applied 3D model allows studying the effects of varying ambient conditions on the heat distribution and temperature of commercial-sized panels. The results show that replacing the standard crystalline silicon with a typical perovskite absorber of ca. 1.6 eV band gap as the active material may significantly reduce the module temperature in normal operation: the modeled average cell temperature of the perovskite module was ca. 7 °C less than that of the silicon module under reference conditions (ambient temperature 20 °C, wind speed 1 m/s, and solar irradiance 800 W/m^2). The novelty of the study is the predicted set of perovskite-module-specific model parameters for the Sandia (a = −3.77, b = −0.129), Faiman (U_{L0} = 37.93 W/m^{2}K, U_{L1} = 10.47 Ws/m^{3}K), PVsyst (U_0 = 19.29 W/m^{2}K, U_1 = 5.27 Ws/m^{3}K), Mattei ($U_{PV} = 4.49v + 16.65$, v is the wind speed), and TRNSYS ($U_{Loss} = 4.54v + 16.38$) models that were determined by fitting these models to the simulated temperature data in the varying ambient conditions. These parameters enable estimation of perovskite panel temperature in varying outdoor conditions with existing PV system models.

1. Introduction

Perovskite solar cells (PSCs) are promising for photovoltaic (PV) applications due to their high power conversion efficiency (PCE), tunability of material composition and band gap, short energy payback time, and potential for low-cost fabrication [1]. For example, high-efficiency minimodules have been realized with certified efficiencies, reaching as high as 22.4 ± 0.5% and 18.6 ± 0.7%, respectively, for minimodules (10 − 200 cm^2) and small modules (800 − 6500 cm^2) [2]. There is very active research on the key issues of improving stability and developing upscaling [3]. As the technology advances toward commercialization, there is an interest in developing, for example, performance assessment models for perovskite solar devices that align with commercial softwares used for silicon solar panels, such as PVsyst [4], to provide insights into the power production during the panel lifetime. A common choice for considering PV efficiency dependence on cell temperature is semi-empirical temperature models, which require cell-specific model parameters [5–11]. Due to the current development stage of perovskite technology, there are limitations in the long-term temperature measurements of perovskite panels required to produce semi-empirical temperature model parameters. Thus, this study predicts the temperature model parameters for perovskite panels based on the modeled data.

For commercial PV systems, it is important to predict their power production, which is inherently dependent on the weather due to variations in solar irradiation. Further, module operating temperature affects the efficiency of solar cells [12], causing additional dependence on the ambient conditions. The temperature dependent module performance models allow the system designers to account the effect of varying operation conditions to the PV energy yield unlike the standard test condition ratings that are only useful for estimating the peak performance of the system [13]. In addition, understanding the operating

* Corresponding author.
E-mail address: aleksi.kamppinen@utu.fi (A. Kamppinen).

https://doi.org/10.1016/j.solmat.2025.113657
Received 29 January 2025; Received in revised form 3 April 2025; Accepted 18 April 2025
Available online 9 May 2025

Nomenclature

α	Spectral absorption coefficient
α_{tot}	Total absorption coefficient
β_{Eg}	Temperature dependence of band gap (meV/K)
β_T	Temperature coefficient of efficiency
ϵ	Surface emissivity
η_e	Electrical efficiency
λ	Wavelength (nm)
PCE_{ref}	Reference power conversion efficiency
ρ	Density (kg/m^3)
σ	Stefan–Boltzmann constant
$\vec{n}$	Normal vector of the boundary
$\vec{q}$	Heat flux (W/m^2)
A	Constant component of U_{PV} (W/m^2K)
a	Sandia model parameter (constant)
B	Wind coefficient of U_{PV} (Ws/m^3K)
b	Sandia model parameter (wind coefficient)
c_p	Specific heat capacity (J/kgK)
E_g	Band gap (eV)
G	Plane-of-array irradiance (W/m^2)
G_λ	Solar irradiance spectrum (W/m^2)
G_{ref}	Reference plane-of-array irradiance (W/m^2)
h	Convective heat transfer coefficient (W/m^2K)
K	Thermal conductivity (W/mK)
k_B	Boltzmann constant
L	Layer thickness (μm)
L_{cell}	Cell thickness (m)
n	Ideality factor of the cell
Q	Heat generation (W/m^3)
q	Elementary charge
T	Temperature (°C)
T_{amb}	Ambient temperature (°C)
T_{cell}	Cell temperature (°C)
T_m	Module temperature (°C)
T_{ref}	Reference temperature (°C)
U_{L0}	Faiman model parameter (constant) (W/m^2K)
U_{L1}	Faiman model parameter (wind coefficient) (Ws/m^3K)
U_{Loss0}	Constant component of U_{Loss} (W/m^2K)
U_{Loss1}	Wind coefficient of U_{Loss} (Ws/m^3K)
U_{Loss}	TRNSYS model parameter (W/m^2K)
U_{PV}	Mattei model parameter (W/m^2K)
U_0	PVsyst model parameter (constant) (W/m^2K)
U_1	PVsyst model parameter (wind coefficient) (Ws/m^3K)
v	Wind speed (m/s)
$V_{OC,ref}$	Open circuit voltage of the cell in T_{ref} and G_{ref}

temperature is expected to be more critical for PSCs than traditional solar panels, such as silicon, because the stability of PSCs is negatively impacted by high module temperatures [14–17]. Therefore, high temperatures are particularly undesirable in perovskite solar modules.

The module operating temperature depends on multiple factors that can be categorized as ambient conditions, such as the temperature, wind speed, and solar irradiance, as well as design factors that include, for instance, the installation, module design, and active material properties [18–21]. The effects of ambient conditions and design factors on the operating temperature can be modeled with physical device models based on thermal device physics (that is, heat generation and transfer) and material properties [18,19,22–24]. Alternately, (semi-)empirical models can be applied to predict the module temperature directly from the ambient conditions. In this other group of models, a mathematical expression is formulated and the model parameters include the information on the heat generation in the module and heat transfer from the module to the environment [5–11].

Several semi-empirical models that predict the temperature of PV modules with respect to the ambient conditions are described in the literature [5–10,21,25–30]. Such models are easy to apply and integrate into large-scale system models to account for the impacts of weather on PV systems. However, the model parameters may depend on, for example, the module type and installation, and they need to be determined experimentally or computationally for a specific case [5,31]. Most of these models include the effect of varying wind speeds on the module operating temperature [5–9,25,28–30]. However, especially the older temperature models often ignore the wind speed [10,21,26,27]. The temperature estimation accuracy of models including wind speed has been reported to be notably higher in comparison with models that do not take wind speed into account [21]. This study predicts model parameters to be used for a perovskite solar panel with the Sandia [5], Faiman [6], PVsyst [7], Mattei [8], and TRNSYS [9–11] models, based on simulations with our physical device model including the thermal processes. These five models are investigated in more detail as they include the effects of wind speed and are well established in PV module modeling [10,21,31].

Some research has been conducted on the heat distribution in PSCs [32–34]. In these studies, the heat distribution within the solar cell is investigated through COMSOL Multiphysics, which is a numerical simulation software that can be used to model, for instance, temperature and heat transfer. The electrical behavior, optical absorption, and heat conduction and convection are considered to understand the vertical heat distribution across the PSC layers [32,33]. In addition, the effect of the bottom electrode material on the thermal behavior of the cell is discussed [32,34]. Thermal models that study the temperature of an individual PSC under steady state and changing environmental conditions are also presented in the literature [35–37]. However, studies on the operating temperature of commercial-scale perovskite solar panels are scarce. As shown by thermal studies of silicon panels, temperature varies in the modules in horizontal dimensions [19,22]. Importantly, the literature lacks the perovskite-specific model parameters for the considered module temperature models.

In the literature, several thermal models study the temperature and the heat distribution of silicon PV panels in various ambient conditions [18,19,22,23]. However, a typical perovskite absorber has, for example, a notably larger band gap compared with silicon. The larger band gap is expected to result in reduced heat generation within the panel [20] and, hence, in a lower operating temperature of the panel [20,37]. Thus, the hypothesis in this study is that the existing model parameters of the current module temperature models do not accurately predict the operating temperature of a perovskite panel. The aim is to find more suitable parameters by computational simulation.

In this study, the heat distribution and temperature of perovskite solar panels are investigated using COMSOL Multiphysics and compared with silicon solar panels. The effects of ambient temperature, wind speed, and solar irradiance on the module temperature are considered. The thermal model presented in this study was validated using experimental data from a silicon solar panel. Common PV temperature models, namely the Sandia, Faiman, PVsyst, Mattei, and TRNSYS models, are fitted into the computationally simulated temperature data

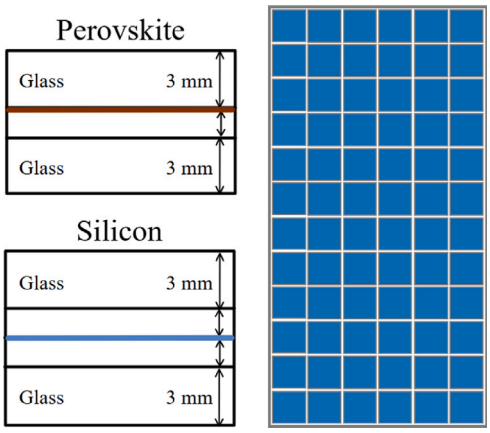

Fig. 1. Illustration of the solar module design (right) and the components in the silicon and perovskite modules (left).

in varying conditions, and the model parameters are obtained for and compared with different panel types. Therefore, the results predict perovskite-panel-specific model parameters that are required to simulate the panel temperature with the aforementioned PV temperature models. The new parameters enable the easy implementation of perovskite panel thermal modeling in PV system models that already apply these temperature models by the use of a simple parameter change. The panel type specific parameters can improve the perovskite panel temperature estimation, thus benefiting system design and power production estimation in outdoor conditions.

2. Methods

2.1. Model geometry and material properties

To study the temperature and heat distribution of the perovskite and silicon modules, three-dimensional (3D) COMSOL models were applied. The codes for running the simulations are openly available [38]. The 3D models of both modules are equal in size to allow direct comparison. The size of an individual cell is 15.6 cm × 15.6 cm, and the distance between adjacent cells is 1 cm. The dimensions of the whole module are 200.2 cm × 100.6 cm. The perovskite module consists of a back glass, ethylvinylacetate (EVA), PSCs, and a front glass. The silicon module consists of a back glass, EVA, silicon solar cells, and a front glass. In the perovskite module, the cells are placed between the front glass and EVA, whereas in the silicon module, the cells are placed between two EVA layers. One EVA layer is 0.5 mm, and both the front and back glass layers are 3 mm thick in all cases. The solar module design and components of both module types are shown in Fig. 1. It should be noted that both silicon and perovskite panels are monofacial despite the back surface glass. The applied panel structure is based on the silicon panel that was used for model validation, and the same structure is considered for the perovskite panel for comparability. The monofaciality is due to the metallic back contact of the cells. Despite the fact that the back surface material could affect the module temperature via altered back surface cooling, the effect is expected to be similar for both panel types, and thus, the relative difference between the temperatures of the two panel types is expected to generalize quite well with different back surface materials.

The modeled PSCs consist of Au, Spiro-OMeTAD, $MAPbI_3$, TiO_2, and FTO layers. However, these individual layers of PSC are very thin, usually varying from 50 nm to 500 nm. Therefore, it is impractical to model each layer of the PSCs separately because of the large aspect ratio between different dimensions considering the size of the solar module. In this case, all perovskite cell layers are treated as a uniform material and modeled as one thin film layer. The silicon solar cells are also modeled as a thin film layer. The material properties and layer thicknesses set for the thermal models of perovskite and silicon solar modules (Table 1) are based on literature values and a separate PSC model that was applied to study the properties of the artificial, uniform PSC layer. The details of the PSC layer model are described in the Supporting Information Section 1.

Table 1
Material properties of glass, EVA, PSC, and silicon, and the thicknesses of glass and EVA.

	Glass [19]	EVA [19]	PSC	Silicon [19]
K [W/(mK)]	2	0.311	[33, 33, 1][a]	130
ρ [kg/m^3]	2450	950	5620.3	2330
c_p [J/(kgK)]	500	2090	305.7	677
L [mm]	3	0.5	–	–

[a] Thermal conductivity of PSC is anisotropic due to its multilayer structure. The conductivity is given in [x, y, z] directions.

2.2. Heat transfer

The temperature profiles of the modules are determined by Fourier's law of heat conduction

$$\vec{q} = -K\nabla T, \tag{1}$$

where $\vec{q}$ is the heat flux, K is the thermal conductivity, ∇ is the gradient operator, and T is the temperature, and the heat equation which states that, in steady state,

$$Q + K\nabla^2 T = 0, \tag{2}$$

where $Q = \nabla \cdot \vec{q}$ is the heat source.

Basic heat transfer modes are convection, conduction, and radiative heat transfer. Convection is a significant heat transfer mode between the module and its environment [19]. Including convection in the thermal model is essential, especially when the aim is to study model temperatures in varying outdoor conditions. This study applies a forced convection coefficient that depends on wind speed, unlike free convection. In some cases, for example, in very low wind speeds, free convection may be relevant to the modeling [39]. However, Notton et al. [39] concluded that considering free convection does not improve the performance of the model. Further, the forced convection coefficient offers similar values in calm wind conditions to the free convection coefficient [24]. The coefficient would not be zero even if the wind speed was zero. In this model, convective heat flux is applied to all external surfaces, and it is defined by Eq. (3) [40]:

$$-\vec{n} \cdot \vec{q} = h(T_{amb} - T_m), \tag{3}$$

where $\vec{n}$ is the normal vector of the boundary, $\vec{q}$ is the convective heat flux, h is the convective heat transfer coefficient, T_{amb} is the ambient temperature, and T_m is the module surface temperature.

The convective heat transfer coefficient is defined according to Eq. (4) [41]:

$$h = 2.8\left(\frac{\mathrm{W}}{\mathrm{m^2K}}\right) + 3\left(\frac{\mathrm{Ws}}{\mathrm{m^3K}}\right) v, \tag{4}$$

where v is the wind speed. The convective heat transfer coefficient's dependence on the wind speed can be utilized to investigate the effect of wind speed on the module temperature. On the back and side surfaces of the module, h is assumed to be half of that on the front surface to account for reduced cooling on the back side [19,42]. However, it seems that only the effective convective coefficient matters for cooling. That is, it does not matter whether the coefficients are larger, smaller or equal to each other on the front and back sides but, rather, the sum of the applied coefficients (Figure S3). Several alternatives to the heat transfer coefficient are presented in the literature, and the choice of appropriate coefficient is influenced, for example, by the mounting structure and tilt angle of the module [43].

The selected coefficient for convection excludes the radiation term [41,44]. Instead, radiation from the panel surfaces to the environment is determined as inward heat flux by Eq. (5) [40]:

$$-\vec{n}\cdot\vec{q} = \epsilon\sigma(T_{\mathrm{amb}}^4 - T_{\mathrm{m}}^4), \tag{5}$$

where $\epsilon = 0.85$ is the surface emissivity and σ is the Stefan–Boltzmann constant.

2.3. Heat generation

Heat generation is defined as

$$Q(G, T_{\mathrm{cell}}) = \frac{(1-\eta_{\mathrm{e}}(G, T_{\mathrm{cell}}))\,\alpha_{\mathrm{tot}}(T_{\mathrm{cell}})\,G}{L_{\mathrm{cell}}}, \tag{6}$$

where G is the plane-of-array (POA) irradiance, T_{cell} is the cell temperature, η_{e} is the electrical efficiency, α_{tot} is the total absorption coefficient, and L_{cell} is the cell thickness (the unit of heat production is power per volume) [19]. α_{tot} is determined as a weighted average of spectral absorption where the weighting factor is the spectral irradiance of a global AM1.5 spectrum [45]. η_{e} and α_{tot} determine the electrical and optical operation, respectively, to account for the different types of losses separately. The total absorption coefficient is the fraction of solar irradiance that is absorbed by the cell including all the layers, and it depends on the temperature due to the band gap temperature dependence. The heat source is applied to the cell layers because that is where the energy conversion, both to electricity and heat, occurs.

The most significant difference between silicon and PSCs, from a thermal point of view, is expected to arise from their different band gaps, because the band gap (E_{g}) largely determines absorption and thermalization, and, thus, heat generation in the cells [20,46,47]. Therefore, α_{tot} and η_{e} are defined as functions of E_{g} in the spirit of Ref. [45]

$$\alpha_{\mathrm{tot}}(T_{\mathrm{cell}}) = \left[\int_{300\,\mathrm{nm}}^{\lambda_{\mathrm{g}}(T_{\mathrm{cell}})} \alpha_{\lambda<\lambda_{\mathrm{g}}}\, G_\lambda\, d\lambda + \int_{\lambda_{\mathrm{g}}(T_{\mathrm{cell}})}^{4000\,\mathrm{nm}} \alpha_{\lambda\geq\lambda_{\mathrm{g}}}\, G_\lambda\, d\lambda\right] \Big/ \int_{300\,\mathrm{nm}}^{4000\,\mathrm{nm}} G_\lambda\, d\lambda \tag{7}$$

$$\eta_{\mathrm{e}}(G, T_{\mathrm{cell}}) = \frac{\mathrm{PCE}\,(G, T_{\mathrm{cell}})}{\alpha_{\mathrm{tot}}(T_{\mathrm{cell}})}, \tag{8}$$

where G_λ is the solar irradiance spectrum and λ_{g} is the wavelength corresponding to $E_{\mathrm{g}} = E_{\mathrm{g}}(T = 25\,^{\circ}\mathrm{C}) + \beta_{E\mathrm{g}}(T_{\mathrm{cell}} - 25\,^{\circ}\mathrm{C})$, where $\beta_{E\mathrm{g}}$ is the temperature dependence of the band gap [48,49]. Spectral absorption coefficients $\alpha_{\lambda<\lambda_{\mathrm{g}}} = 0.95$ and $\alpha_{\lambda\geq\lambda_{\mathrm{g}}} = 0.2$ in the absorption integrals define that 95% or 20% of irradiance, respectively, is absorbed if the corresponding photon energy is above or below the band gap. The spectral absorption coefficient of 0.95 was chosen based on the low reflectance of around 5% for above band gap energy range reported for both silicon [50] and perovskite [51] solar cells. The spectral absorption coefficient of 0.2 for below band gap irradiation defines the parasitic absorption due to absorption especially in the back reflector/electrode [50]. $\mathrm{PCE}_{\mathrm{ref}}$ is the reference power conversion efficiency (in $T_{\mathrm{ref}} = 25\,^{\circ}\mathrm{C}$ and $G_{\mathrm{ref}} = 1000\,\mathrm{W/m^2}$) and is defined to be 20% for both module types. Otherwise, the temperature and irradiance dependence of PCE [12,52–55] is considered by defining (see Supporting Information Section 2)

$$\mathrm{PCE}\,(G, T_{\mathrm{cell}}) = \mathrm{PCE}_{\mathrm{ref}}\left[1 + \frac{nk_{\mathrm{B}}T_{\mathrm{ref}}}{V_{\mathrm{OC,ref}}\,q}\ln\left(\frac{G}{G_{\mathrm{ref}}}\right)\right](1 + \beta_{\mathrm{T}}(T_{\mathrm{cell}} - T_{\mathrm{ref}})), \tag{9}$$

where n is the ideality factor of the cell, k_{B} is the Boltzmann constant, $V_{\mathrm{OC,ref}}$ is the open circuit voltage of the cell in reference temperature and irradiance, q is the elementary charge, and β_{T} is the temperature coefficient of efficiency. The first term in parentheses in Eq. (9) represents the irradiance dependence based on the V_{OC} irradiance dependence. The fill factor is also susceptible to change under varying irradiance, but it depends on several panel-specific parameters, such as series resistance, which are not necessarily directly linked to the choice of active material, and it is, therefore, omitted. The second term in parentheses represents the temperature dependence of PCE and it is based on literature values describing the difference in PCE under temperature change with the two active materials. The model parameters for both module types are summarized in Table 2.

The choices of optical and electrical models aim to capture the essential differences between perovskite and silicon solar cells. Different module and cell design aspects, including a set of material parameters and the device architecture defining the electrical operation of each cell, are expected to affect, for example, α_{tot}, $\eta_{\mathrm{e,ref}}$, and, therefore, Q; however, this goes for both module types, and the aim here is to perform a temperature comparison between the module types as equivalently as possible by focusing on their fundamental differences. Different band gaps cause differences in heat generation, and different temperature coefficients lead to the panels responding differently to the increasing cell temperature. Amendments leading to improved accuracy with a loss of generality are possible and encouraged when conducting further research for a specific module; however, the presented key properties should not be neglected.

2.4. Model validation

The thermal model described above was validated using on-site weather and PV temperature data collected from the Finnish Meteorological Institute's (FMI) measurement site in Helsinki [61]. At the measurement site, the PV system consists of monofacial polycrystalline silicon panels (SolarWorld Protect SW 250 poly) that were installed in 2015. The panels are mounted at a tilt angle of 15° and an azimuth angle of 135° on a flat roof at 17 m above ground. The POA irradiance, roof air temperature, air temperature at 2 meters, and module temperature were measured with 1 min resolution while 10 m wind speed was recorded every ten minutes. The module temperature was measured inside insulated capsules from the back surface of the module at the southwest (SW) and northeast (NE) corners of the PV system. The air temperature at 2 meters and wind speed were observed at the nearby weather station. A more detailed description of the experimental data and the characteristics of the PV measurement site are provided by Karhu et al. [61].

The measured POA irradiance, roof air temperature, and wind speed were set as model inputs. The roof air temperature was chosen as the ambient temperature because it describes the conditions around the module more realistically than the air temperature measured at the nearby weather station. The present thermal model was modified to match the reference module at the measurement site of FMI by replacing the initial $\mathrm{PCE}_{\mathrm{ref}}$ and β_{T} with the values reported by manufacturer of the reference module. The periods with a snow cover on the surface of the module were excluded since the thermal model does not consider the effects of snowy conditions. The snow filter removed all observations during which the snow depth on the ground was more than zero to ensure that the surface of the module was snow-free [62]. Measurement data from January to December 2020 (Figure S4) were utilized in the model validation. To save computational resources, the module temperature was not modeled at each point but rather a representative set of data was selected (Figure S5). The number of data points used for the model validation were narrowed down by selecting the points closest to the specified environmental conditions that widely represent possible combinations of ambient temperature, wind speed, and irradiance. The specified environmental conditions include ambient temperatures from 5 °C to 30 °C with steps of 5 °C, wind speeds from 1 m/s to 10 m/s with steps of 1 m/s, and irradiances from 100 W/m^2 to 1000 W/m^2 with steps of 100 W/m^2 and the Euclidean norm was applied to choose the experimental points closest to these points (Figure S5).

Finally, the simulated module temperature was compared with the measured one (Fig. 2). Here, the simulated module temperature refers to the maximum temperature of the module back surface because it is expected to best describe the module temperature at the point where the temperature sensor is placed during the measurement. The

Table 2
Model parameters applied in Eqs. (6)–(9).

	PCE_{ref}	$\alpha_{\lambda<\lambda_g}$	$\alpha_{\lambda\geq\lambda_g}$	$E_g(T = 25\,°C)$	$V_{OC,ref}$	n	β_T	β_{Eg}
Si	20%	0.95	0.2	1.12 eV	0.6 [56,57]	1.3 [56,57]	−0.35 %/K [58]	−0.273 meV/K [48]
PVK	20%	0.95	0.2	1.57 eV	1.1 [59]	1.3 [59]	−0.17 %/K [60]	0.25 meV/K [49]

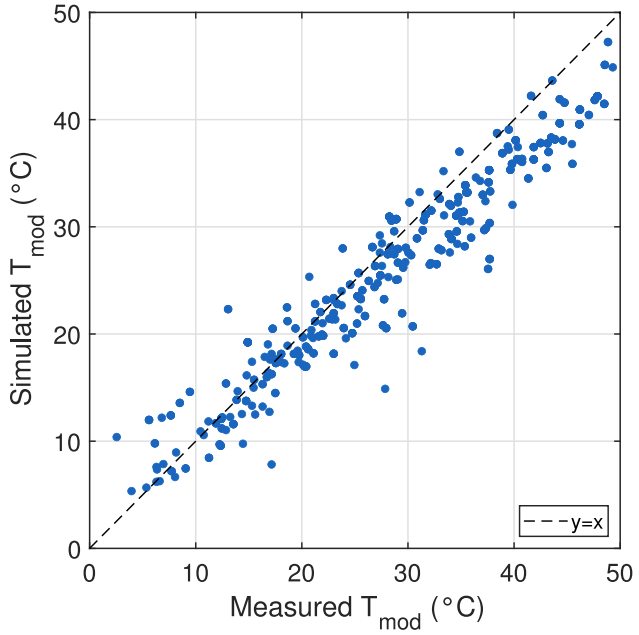

Fig. 2. The simulated module temperature as a function of the average of the module temperatures measured from the SW and NE corners. The dashed line illustrates the ideal relationship between predicted and measured values.

highest temperature of the module back surface is reached at the point corresponding to the center of any cell not located at the edge of the module (Fig. 3) and the temperature of the FMI's panels is measured close to such points [61].

The present thermal model estimates the module temperature with a root mean square error (RMSE) of 4.0 °C, and mean absolute error (MAE) of 3.2 °C. The correlation coefficient is 0.963, which indicates a strong positive correlation between the simulated and measured module temperatures. Altogether, the evaluation metrics demonstrate good performance of the present thermal model.

Furthermore, even better agreement between the simulation and the experiment was achieved when only the temperatures measured from the SW corner of the PV system are included in model validation (Figures S6 and S7). The module temperatures measured from the SW corner showed a good agreement with the simulated maximum temperatures of the module back surface, as the RMSE was 3.2 °C, MAE was 2.3 °C, and correlation coefficient was 0.964 (Figure S6a). Additionally, a reasonable agreement between the measured data and the simulated average temperature of the module back surface was found (Figure S6b). The more accurate model prediction based on the temperatures measured from the SW corner is likely due to the wind flow conditions on the roof of the FMI's site. At the SW corner of the PV system the wind can flow more freely along the panel array, whereas at the NE corner there are more obstacles. Furthermore, the actual wind speed on the surface of the module is likely to be lower compared with the measured wind speed because the wind can flow more freely at the wind measurement station than on the roof on which the PV system is installed. Uncertainty analysis showed that the applied factor of wind speed in the convective heat transfer coefficient (Eq. (4)) is probably too large for the specific installation because $k = 2$ (instead of $k = 3$) provided better agreement with the experimental data (Figure S8 and Table S2).

The validation with experimental data shows that the present thermal model predicts the operating temperatures of the silicon module in varying conditions well. As mentioned, the boundary conditions of the thermal model were similar for both silicon and perovskite modules. Thus, the differences in the module operating temperatures arise from the material properties of the silicon and perovskite cells and not from the physics of the heat transfer model. Consequently, it is considered that the model predicts the temperature of the perovskite module equally well.

3. Results and discussion

Initially, the module temperature at the maximum power point (MPP) was calculated in reference weather conditions similar to the basic nominal module operating temperature (NMOT) conditions, that is, solar irradiance of 800 W/m^2, an ambient temperature of 20 °C, and a wind speed of 1 m/s [63,64]. The temperature of the perovskite module was found to be lower than the temperature of the silicon module in the reference conditions, as shown in Fig. 3(a). The operating temperatures of both modules were observed through the fourth cell row from the top, indicated in Fig. 3(c), at the cell surface level. The difference between the perovskite and silicon module temperatures arises from the wider band gap of the perovskite. The wider band gap decreases absorption and thermalization and, consequently, heat generation.

The highest temperature of the perovskite solar module was 38.0 °C, the average module temperature was 35.9 °C, and the average cell temperature was 36.4 °C, whereas the highest temperature of the silicon solar module was 45.3 °C, the average module temperature was 42.2 °C, and the average cell temperature was 43.2 °C. Here, the cell temperature refers to the average temperature of all 72 cells, and the module temperature refers to that of all module domains. The average temperature of the module was lower than the average temperature of the cells, because there is no heat generation in the module components other than the cells. The temperature reached its highest value in the centers of the cells and the lowest at the outer edge of the module. The temperature also decreased toward the edges of the cells, and the variation was regular through the module (Fig. 3). It is noteworthy that the average temperature of the individual cells remained almost the same, regardless of their location in the module. Only in the outermost cells was the average temperature around 0.5 °C lower in comparison with the other cells for both module types. The results appear realistic: the temperature of the perovskite layer in the reference conditions is reported to vary between 36 °C and 42 °C, depending on the installation [35]. For crystalline silicon, the module temperature at the MPP is reported to vary between 42 °C and 46 °C under the same conditions [31].

Uncertainty analysis was conducted by varying below band gap absorption ($\alpha_{\lambda\geq\lambda_g}$, see Table 2) from 0 to 0.4. The average cell temperature in the reference conditions subsequently varied from 33.3 to 39.5 °C and from 41.8 to 44.6 °C, respectively, for perovskite and silicon panels (Figure S9). $\alpha_{\lambda\geq\lambda_g}$ affected the operating temperature substantially, because all below band gap absorption becomes heat. It cannot be entirely eliminated either, for example, due to free electron absorption in the contacts. Large $\alpha_{\lambda\geq\lambda_g}$ increased especially the perovskite temperature because of the larger band gap and wider below band gap range. Nevertheless, perovskite temperature was smaller across the entire range.

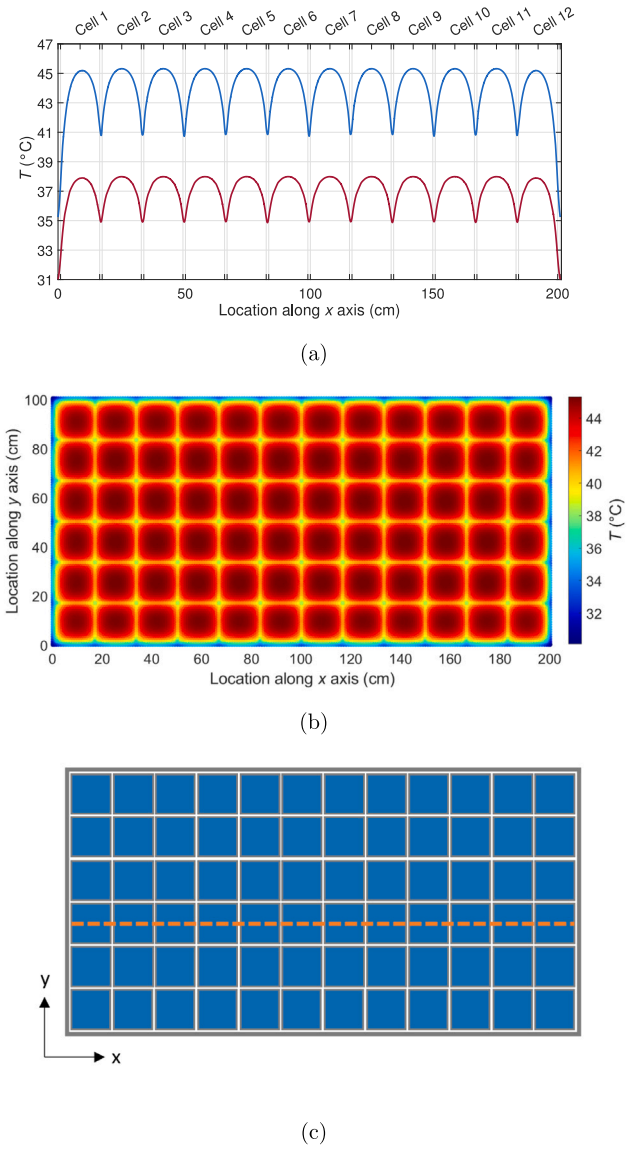

Fig. 3. (a) Temperature distribution in the perovskite (red) and silicon (blue) modules in the reference conditions through the module, along the red dotted line marked in figure part (c) representing the module cross-section. (b) Two dimensional temperature distribution of the silicon module cross-section at the cell surface level within the module (modeled in the reference conditions). (c) Illustration of the module cross-section.

3.1. The effect of ambient conditions on module temperature

The ambient temperature ranged from −20 °C to 50 °C, and this range is expected to cover most ambient temperatures throughout the year in different geographical locations. Within the selected range, the average cell temperature increased from −0.4 °C to 64.3 °C for perovskite cells and from 6.7 °C to 70.6 °C for silicon cells (Fig. 4(a)). Comparable results have been presented in thermal analyses of silicon solar modules [19,22]. Siddiqui et al. [22] reported that the temperature of the silicon cell increased by 47.8 °C (45.6 °C in the present study) when the ambient temperature increased from 0 °C to 50 °C. Because the model provides module temperatures similar to those presented in previous studies for the silicon module, it is reasonable to assume that the results are plausible for the perovskite module as well. The average temperature of the cells rose almost linearly as the ambient temperature increased (Fig. 4(a)) because, according to Eq. (3), if the heat generation is assumed to be constant, the convective heat flux decreases with the increasing ambient temperature. The effect was similar for both module types: the rate of change was 0.92 °C/°C for perovskite and 0.91 °C/°C for silicon in both average and maximum temperatures. However, the effect of ambient temperature is not fully linear in reality, because Eq. (5) for the surface-to-ambient radiation is non-linear and heat generation is also a function of temperature (Eq. (6)).

When the wind speed increased from 0 to 10 m/s, the cell temperature of both the perovskite and silicon decreased rapidly at first, but the temperature-lowering effect began to slow down at higher wind speeds (Fig. 4(b)). At a wind speed of 0 m/s (Fig. 4(b)), the average temperature of the perovskite cells was 41.0 °C while that of the silicon cells was 49.4 °C. As the wind speed increased, the absolute temperature difference between the PSCs and silicon cells decreased. At a wind speed of 10 m/s, the average temperature of the PSCs was 25.6 °C while that of the silicon cells was 28.2 °C. The average temperature of the perovskite and silicon cells decreased by 15.4 °C and 21.2 °C, respectively, as the wind speed increased from 0 to 10 m/s. These results are in line with the dependence of the convective heat transfer coefficient on the wind speed. That is, the convection coefficient increases linearly with the wind speed (Eq. (4)). However, convective heat transfer also depends on the temperature difference between the cell and the ambient (Eq. (3)). Therefore, the actual temperature decrease of the panel with the increasing wind speed slows down when approaching the constant ambient temperature. The cell type did not affect surface cooling, as the heat transfer coefficient was defined similarly for both.

The temperature of both the PSCs and the silicon cells increased as the solar irradiance increased from 100 to 1200 W/m^2 (Fig. 4(c)) in line with the increasing heat generation (Eq. (6)). The average temperature of the PSCs rose from 22.2 °C to 44.1 °C within the modeled range. The average temperature of the silicon solar cells reached 54.0 °C at an irradiance level of 1200 W/m^2. The increase in the temperature of the perovskite cells was significantly lower in comparison with the increase in the temperature of the silicon cells. Considering the average cell temperature, the rate of change was 0.020 °C/(W/m^2) for the perovskite and 0.028 °C/(W/m^2) for the silicon. In the case of the maximum cell temperature, the rate of change was 0.022 °C/(W/m^2) for the perovskite and 0.031 °C/(W/m^2) for the silicon. The lower change of rate of the perovskite cell temperature indicates that the perovskite module heats less than the silicon module, which would be an advantage in high irradiance conditions.

The combined effect of different ambient conditions, such as simultaneous high solar irradiance and low wind speed, led to considerably high operating temperatures of both the perovskite and the silicon cells (Figure S10). For example, at an ambient temperature of 40 °C, a wind speed of 0 m/s, and solar irradiance of 1200 W/m^2, the average temperature of the perovskite cell was 67.1 °C and that of the silicon cell was 78.4 °C. At the same solar irradiance but at an ambient temperature of 0 °C and wind speed of 10 m/s, the cell temperature decreased by 58.6 °C and 66.2 °C for the perovskite and silicon, respectively (Figure S10).

The physics of heat transfer govern the relationship between panel temperature and the ambient conditions. Of the three modes of heat transfer, convection and radiation dominate heat exchange between the panel and its surroundings within normal PV operating temperatures. The two were of the same order of magnitude: radiation was larger at low wind speed while convection increased and became dominant at higher wind speeds (Figure S11). Ambient temperature affects both convection (Eq. (3)) and radiation (Eq. (5)) and wind speed affects convection via heat transfer coefficient (Eq. (4)). Thus, wind speed and ambient temperature define the passive cooling rate of a panel. Overall, irradiance determines how much energy a panel receives, material properties determine how much is converted to heat, and ambient temperature and wind speed determine the cooling.

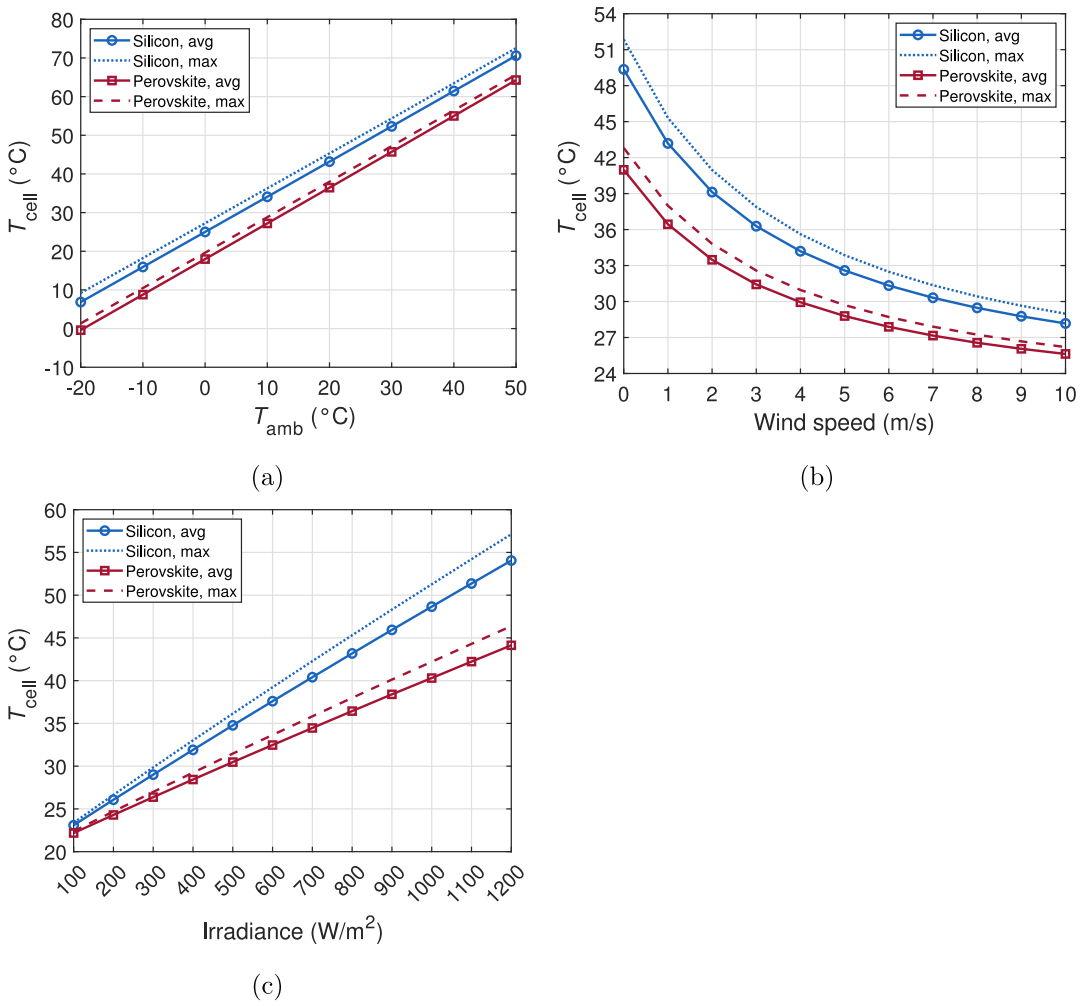

Fig. 4. The effect of (a) ambient temperature, (b) wind speed, and (c) solar irradiance on the average and maximum temperatures of perovskite and silicon cells. The following conditions were applied except the varied parameter: $T_{amb} = 20\,°C$, 1 m/s wind speed, and 800 W/m^2 irradiance (a–c). The lines are guides for the eye.

3.2. Model parameters of common PV temperature models for perovskite

In this study, computationally simulated module temperature data under varying conditions were applied to the Sandia, Faiman, PVsyst, Mattei, and TRNSYS module temperature models to determine the model parameters for a perovskite solar module. The model parameters are expected to be specific to module types; therefore, they were evaluated separately for the perovskite and silicon modules from the modeled data. Once the model parameters are determined, the module temperature can be estimated as a function of the ambient temperature, solar irradiance, and wind speed [5,31]. Furthermore, the module temperature can be used to predict the efficiency, and, thus, estimate the power production of the module.

The procedure of fitting the module temperature models into simulated model temperature data to gain the model parameters was validated with the same experimental data as the 3D thermal model itself was validated. The Sandia, Faiman, and Mattei models were fitted with simulated module temperature data that were produced by applying the 3D silicon panel model in different conditions (figure S12). The Sandia, Faiman, and Mattei models and the model parameters, acquired by the fits, were then applied to estimate the module temperature, and the estimated module temperatures were compared with the experimental data and predictions obtained by the same models using literature parameter values (Figure S13 and Table S3). The parameters obtained by the fits into the simulated panel temperature data produced only slightly less accurate predictions compared with the literature parameters (Table S3), which is a good result because no parameters were fitted here in the physical 3D thermal model itself. Therefore, the physical 3D thermal model can be used to generate credible simulated module temperature data for fitting the other models in the event that experimental data are not available.

The Sandia (Eq. (10)) [5], Faiman (Eq. (11)) [6], PVsyst (Eq. (12)) [7], Mattei (Eq. (13)) [8], and TRNSYS (Eq. (14)) [9–11] models estimate the module temperature according to Eqs. (10)–(14):

$$T_m = T_{amb} + G\exp(bv + a) \tag{10}$$

$$T_m = T_{amb} + \frac{G}{U_{L1}v + U_{L0}} \tag{11}$$

$$T_m = T_{amb} + \frac{G\alpha_{tot}(1 - PCE_{ref})}{U_1 v + U_0} \tag{12}$$

$$T_m = \frac{U_{PV}T_{amb} + G[\alpha_{tot} - PCE_{ref} - \beta PCE_{ref}T_{ref}]}{U_{PV} - \beta PCE_{ref}G} \tag{13}$$

$$T_m = T_{amb} + \alpha_{tot}\frac{G}{U_{Loss}}\left(1 - \frac{PCE_{ref}}{\alpha_{tot}}\right), \tag{14}$$

where a and b, U_{L0} and U_{L1}, U_0 and U_1, $U_{PV} = Bv + A$, and $U_{Loss} = U_{Loss1}v + U_{Loss0}$ are the model parameters of the respective models. The linear forms of Sandia (Eq. (15)), Faiman (Eq. (16)), PVsyst (Eq. (17)), Mattei (Eq. (18)), and TRNSYS (Eq. (19)) are expressed as

$$\log[(T_m - T_{amb})/G] = bv + a \tag{15}$$

$$\frac{G}{T_m - T_{amb}} = U_{L1}v + U_{L0} \tag{16}$$

Table 3
Parameters for the Sandia, Faiman, PVsyst, Mattei, and TRNSYS models using computationally simulated temperature data.

		Perovskite			Silicon		
		Back surface min.[a]	Back surface max.[a]	Cell average	Back surface min.[a]	Back surface max.[a]	Cell average
Sandia	b	−0.148	−0.132	−0.129	−0.146	−0.129	−0.125
	a	−3.86	−3.70	−3.77	−3.52	−3.36	−3.43
Faiman	$U_{L1}[\frac{Ws}{m^3K}]$	14.34	10.12	10.47	9.96	6.93	7.15
	$U_{L0}[\frac{W}{m^3K}]$	39.43	35.19	37.93	28.42	25.28	27.17
PVsyst	$U_1[\frac{Ws}{m^3K}]$	7.44	5.15	5.27	6.54	4.46	4.54
	$U_0[\frac{W}{m^2K}]$	19.47	17.74	19.29	17.97	16.31	17.67
Mattei	$B[\frac{Ws}{m^3K}]$	6.34	4.39	4.49	6.11	4.16	4.24
	$A[\frac{W}{m^2K}]$	16.81	15.33	16.65	17.28	15.73	17.01
TRNSYS	$U_{Loss1}[\frac{Ws}{m^3K}]$	6.22	4.39	4.54	6.02	4.19	4.32
	$U_{Loss0}[\frac{W}{m^2K}]$	17.02	15.19	16.38	17.23	15.32	16.47

[a] Back Surface Min./Max. refer to the minimum and maximum temperatures of the panel back surface.

$$\frac{G\alpha_{tot}(1-\mathrm{PCE_{ref}})}{T_m-T_{amb}} = U_1 v + U_0 \quad (17)$$

$$\frac{G[\alpha_{tot}-\mathrm{PCE_{ref}}-\beta\,\mathrm{PCE_{ref}}(T_m-T_{ref})]}{T_m-T_{amb}} = Bv + A \quad (18)$$

$$\frac{\alpha_{tot}G(1-\mathrm{PCE_{ref}}/\alpha_{tot})}{T_m-T_{amb}} = U_{Loss1}v + U_{Loss0}\,. \quad (19)$$

The linearized models were fitted into the simulated average temperature of all the perovskite and silicon cells, respectively, as shown in Figs. 5–9. The slopes of the fitted lines describe the effect of wind speed on the module temperature, and the intercept coefficient defines the upper limit of the module temperature at low wind speeds. The model parameters for both the perovskite and silicon modules are summarized in Table 3.

The parameters for the Sandia model were within the same order of magnitude for both module types (Fig. 5). The model parameter b was −0.129 for the perovskite module and −0.125 for the silicon module when the average cell temperature was used in the model fitting (Table 3). It was expected that parameter b would be almost equal in both cases because the heat transfer coefficient (as a function of wind speed) was defined similarly for both module types. The model parameter a was 9 – 10% smaller for the perovskite module than for the silicon module (Table 3). The smaller value of parameter a indicates the lower temperature of the perovskite module. The obtained parameters for silicon panel agree with previously reported values [5,31]. Koehl et al. [31] reported that $b = -0.13$ and $a = -3.37$ (or $a = -3.38$ in a different year of experiments) in desert and $b = -0.12$ and $a = -3.55$ in mountain weather conditions, respectively. King et al. [5] presented that $b = -0.06$ and $a = -3.47$ for an open rack mounted module with glass/cell/glass structure. Slight differences, especially in parameter b, can arise from the choice of the heat transfer coefficient that describes in the model, for example, the effects of mounting configuration in reality.

The Faiman model parameter U_{L1}, which describes the effect of wind speed, varied more between the different module types than the similar Sandia model parameter b (Table 3). For the perovskite module, $U_{L1} = 10.47\,\mathrm{Ws/m^3K}$ and $U_{L0} = 37.93\,\mathrm{W/m^2K}$ and for the silicon module, $U_{L1} = 7.15\,\mathrm{Ws/m^3K}$ and $U_{L0} = 27.17\,\mathrm{W/m^2K}$ were obtained when applying the model to the average cell temperature data (Fig. 6). The smaller value of the parameter U_{L0} for the silicon module compared with the perovskite module relates to the smaller value of U_{L0} leading to a higher estimated module temperatures. The reported experimental parameters for silicon solar modules [6,31] are similar as the parameters evaluated from the modeled data (Table 3). Faiman studied the temperatures of seven different type of mono- and polycrystalline silicon solar cells experimentally and concluded that on average $U_{L1} = 7.00 \pm 0.55\,\mathrm{Ws/m^3K}$ and $U_{L0} = 24.9 \pm 1.0\,\mathrm{W/m^2K}$ [6]. Koehl et al. [31] evaluated that $U_{L1} = 6.11 - 6.24$ and $U_{L0} = 26.86 - 26.92\,\mathrm{W/m^2K}$ in desert and $U_{L1} = 7.77\,\mathrm{Ws/m^3K}$ and $U_{L0} = 28.04\,\mathrm{Ws/m^3K}$ in mountain conditions. Koehl et al. [31] also evaluated the parameters for amorphous silicon, CIS, and CdTe solar modules based on experimental data, and the results showed that the model parameters change based on the module type, as was the case in the current study as well.

Considering absorption and PCE as separate model parameters reduces the difference in the cooling parameters between different panel types, as indicated by the PVsyst model fit compared with the Faiman model fit (Table 3). $U_0 = 19.29\,\frac{W}{m^2K}$ and $U_1 = 5.27\,\frac{Ws}{m^3K}$ for perovskite and $U_0 = 17.67\,\frac{W}{m^2K}$ and $U_1 = 4.54\,\frac{Ws}{m^3K}$ for silicon were obtained (Fig. 7). Otherwise, models are alike, but Faiman model parameters typically include optical and electrical efficiencies [6] (see Eqs. (16) and (17)).

The fitted Mattei model parameter U_{PV} was almost equal for perovskite and silicon modules: U_{PV} was $21.1\,\mathrm{W/m^2K}$ for the perovskite module and $21.2\,\mathrm{W/m^2K}$ for the silicon module at the wind speed of 1 m/s (based on average cell temperature, Table 3, Fig. 8). Almost equal model parameters for both modules are explained by the same heat transfer coefficient. It is noted that despite the same heat transfer coefficient, different thermal material properties were considered for perovskite and silicon (Table 1). However, the effect of different thermal properties on the absolute temperature difference across the cells is small due to thin cell layers (Figure S14). As U_{PV} was equal for the different module types, the differences between module types in Mattei model are included in model parameters other than U_{PV}, that is, in α_{tot}, β, and $\mathrm{PCE_{ref}}$. The difference between the two panel types is highlighted by α_{tot} which was defined according to Eq. (7) resulting in $\alpha_{tot} \approx 0.63$ for the perovskite and $\alpha_{tot} \approx 0.81$ for the silicon (in the reference temperature of $T = 25\,°C$).

In the literature, U_{PV} is stated to be either 28.9 or $27\,\mathrm{W/m^2K}$ when the wind speed is 1 m/s, depending on whether value of $\alpha\tau$ is optimized or 0.81 [8]. Therefore, the expression of Mattei model parameter is either $U_{PV} = 2.3v + 26.6$ or $U_{PV} = 2.9v + 24.1$ [8]. In the present study, the fitted U_{PV} was significantly lower leading to higher module temperature. It is claimed that Mattei model underestimates the module temperature at high irradiances [21]. The difference between the current and Mattei model is most likely due to the way the heat transfer coefficient is defined. It should be noted that radiative heat transfer is explicitly neglected in Mattei model [8] while it is included in here, which is why the convective cooling coefficients should not be directly compared.

As with the Mattei model, the TRNSYS model parameter U_{Loss} was almost equal for the perovskite and silicon modules (Table 3, Fig. 9). It is logical because TRNSYS and Mattei models are mathematically rather similar (see Eqs. (18) and (19)). Therefore, when applying TRNSYS model for different panel types, the difference in model parameters arises especially in α_{tot}.

When determining the model parameters, it is relevant from which point the temperature of the module is measured for evaluating the parameters. In experimental studies, the temperature is often measured from the back surface with temperature sensors. The modeled

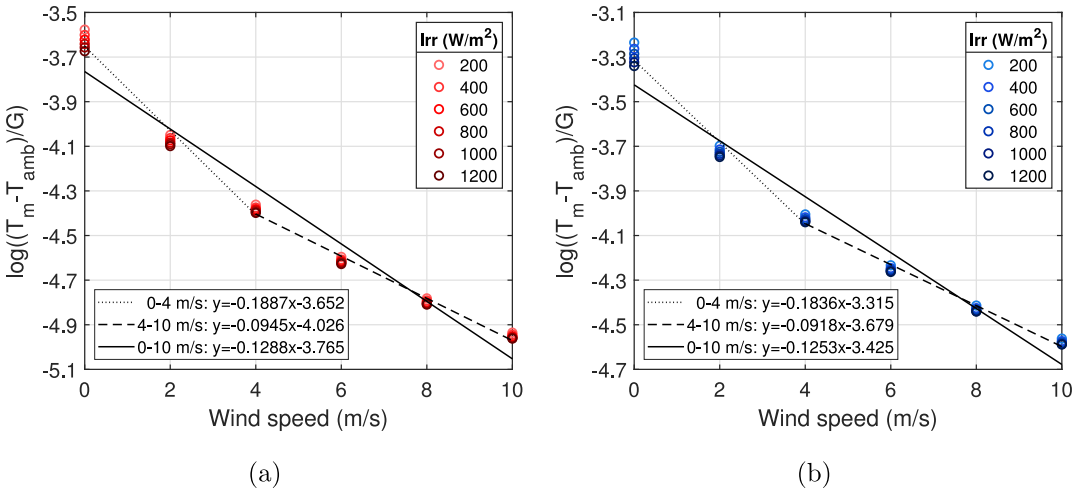

Fig. 5. Linearized form of Sandia model fitted into the average temperature data of (a) perovskite and (b) silicon cells of the respective modules modeled in varying wind speeds and solar irradiances (T_{amb} = 20 °C). The data points for different solar irradiance values are overlapping at all wind speeds. The fits are presented only in the ranges in which they are applicable.

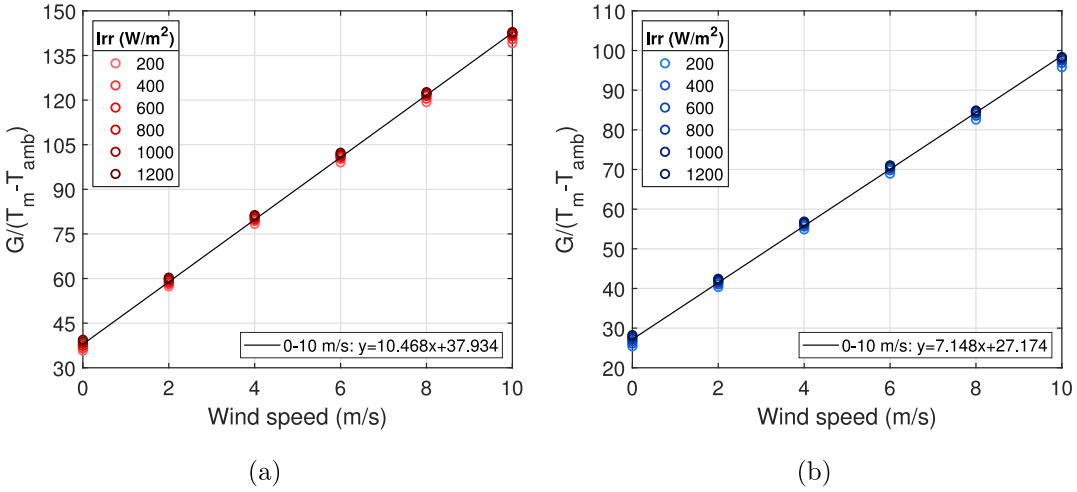

Fig. 6. Linearized form of Faiman model fitted into the average temperature data of (a) perovskite and (b) silicon cells of the respective modules modeled in varying wind speeds and solar irradiances (T_{amb} = 20 °C). The data points for different solar irradiance values are overlapping at all wind speeds.

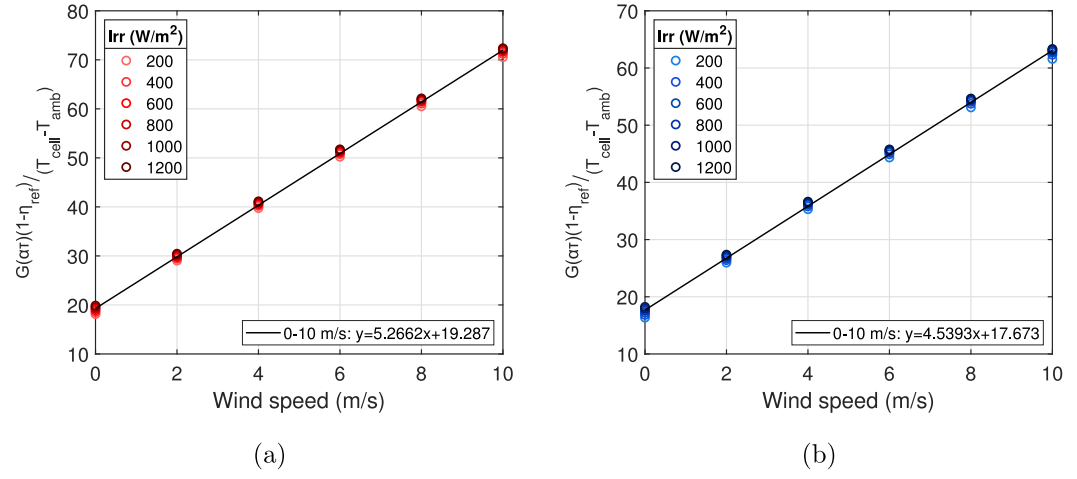

Fig. 7. Linearized form of PVsyst model fitted into the average temperature data of (a) perovskite and (b) silicon cells of the respective modules modeled in varying wind speeds and solar irradiances (T_{amb} = 20 °C). The data points for different solar irradiance values are overlapping at all wind speeds.

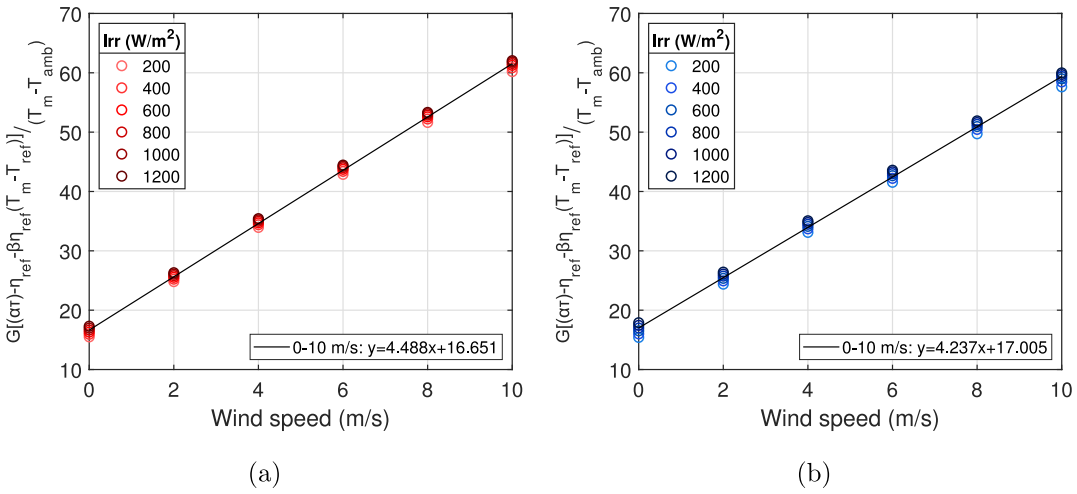

Fig. 8. Linearized form of Mattei model fitted into the average temperature data of (a) perovskite and (b) silicon cells of the respective modules modeled in varying wind speeds and solar irradiances (T_{amb} = 20 °C). The data points for different solar irradiance values are overlapping at all wind speeds.

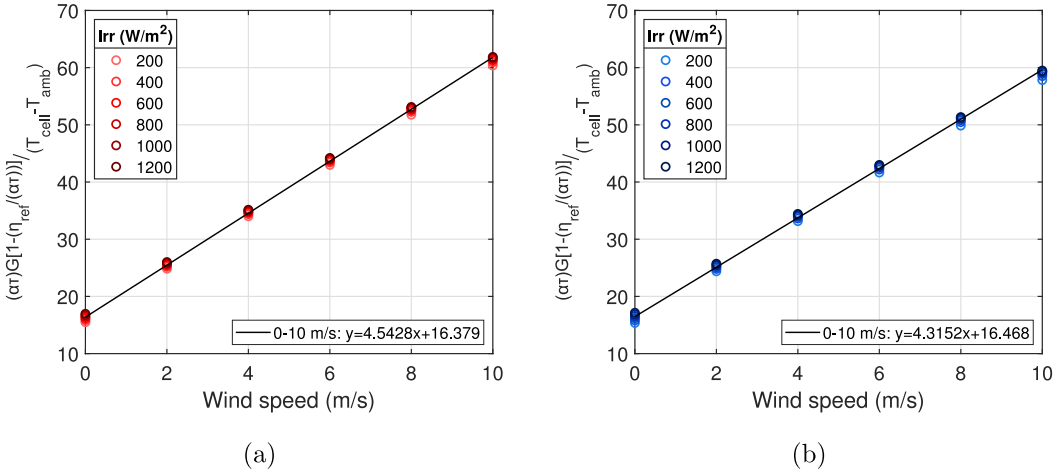

Fig. 9. Linearized form of TRNSYS model fitted into the average temperature data of (a) perovskite and (b) silicon cells of the respective modules modeled in varying wind speeds and solar irradiances (T_{amb} = 20 °C). The data points for different solar irradiance values are overlapping at all wind speeds.

maximum temperature of the module back surface is estimated to be closest to the module temperature measured by temperature sensors in experimental studies. In reality, it is quite challenging to set the temperature sensor exactly where the maximum temperature of the module occurs, which may also explain some differences between the parameters reported in the present study and those reported in the literature. In general, attention should be paid to the location of the temperature sensors in experiments, because the present results showed that the parameters evaluated from the minimum temperature of the back surface lead to notably lower estimated module temperatures compared to using the parameters estimated from the maximum temperatures (Table 3, see Figures S15–S19 for the fits). For example, the estimated module temperature at reference conditions would be 2.8 °C and 4.0 °C lower for the perovskite and silicon modules, respectively, if the Sandia model parameters (Table 3) determined from the minimum temperature of the module back surface were used in temperature estimation, according to Eq. (10), instead of those determined from the maximum temperature.

In practice, the novel model parameters can improve temperature estimation of perovskite panels with the selected module temperature models. Due to temperature dependence of power production, power production estimation and system design may also be developed. In addition, operating temperature is considered in other applications as well, such as temperature corrections for performance ratio [65,66].

Future research could experimentally validate the proposed perovskite-specific model parameters. The effect of different conditions, not considered here, such as different climates and installations [67], could also be studied. Further, a similar approach of simulating the module temperature based on physics modeling may be applied to alternative empirical mathematical formulas for the temperature estimation or other emerging panel types, for example, tandem devices.

4. Conclusions

By conducting thermal simulations of perovskite and silicon solar panels in varying environmental conditions, the present study showed that the temperature of a perovskite module may be lower than that of a silicon module. The obtained temperature difference between the two module types was notable, ca. 7 °C, in ambient conditions corresponding to NMOT conditions. The smaller heat production and slower temperature rise under increasing irradiation would be an advantage for perovskite panels in high irradiance conditions that also provide the highest power production. As another main result, the study predicted the first set of perovskite-panel-specific model parameters for

the Sandia, Faiman, PVsyst, Mattei, TRNSYS module temperature models for predicting thermal behavior of a commercial-scale perovskite module under varying environmental conditions. These parameters can improve perovskite panel temperature estimation in varying outdoor conditions with existing PV system models.

CRediT authorship contribution statement

Julianna Varjopuro: Writing – original draft, Investigation, Formal analysis. **Aleksi Kamppinen:** Writing – original draft, Validation, Supervision, Methodology, Funding acquisition, Conceptualization. **Aapo Poskela:** Writing – review & editing. **Juha A. Karhu:** Writing – review & editing, Investigation. **Anders V. Lindfors:** Writing – review & editing. **Kati Miettunen:** Writing – review & editing, Supervision, Funding acquisition.

Declaration of competing interest

The authors declare that they have no known competing financial interests or personal relationships that could have appeared to influence the work reported in this paper.

Acknowledgments

J.V. and A.V.L. thank RealSolar project (358542, 358543), which is funded by the Strategic Research Council (SRC), Finland established within the Research Council of Finland. A.K. acknowledges funding from Jenny and Antti Wihuri Foundation, Finland, University of Turku Graduate School (UTUGS), Finland, and the Finnish Foundation for Technology Promotion, Finland. K.M. thanks Research Council of Finland (project BioEST, 336577). J.A.K. thanks Fortum and Neste Foundation, Finland.

Appendix A. Supplementary data

Supplementary material related to this article can be found online at https://doi.org/10.1016/j.solmat.2025.113657.

Data availability

Data supporting this study are openly available from repository of Finnish Meteorological Institute at https://doi.org/10.57707/fmi-b2share.fbe73c1d7c144ce787db3785302dd1e1and the codes on Github: https://github.com/juliavarjop/Comparison_of_PVK_and_Si_panel_temperatures.

References

[1] L. Qiu, L.K. Ono, Y. Qi, Advances and challenges to the commercialization of organic–inorganic halide perovskite solar cell technology, Mater. Today Energy 7 (2018) 169–189, http://dx.doi.org/10.1016/j.mtener.2017.09.008.

[2] M.A. Green, E.D. Dunlop, M. Yoshita, N. Kopidakis, K. Bothe, G. Siefer, X. Hao, Solar cell efficiency tables (Version 63), Prog. Photovolt., Res. Appl. 32 (1) (2024) 3–13, http://dx.doi.org/10.1002/pip.3750.

[3] P. Zhu, C. Chen, J. Dai, Y. Zhang, R. Mao, S. Chen, J. Huang, J. Zhu, Toward the commercialization of perovskite solar modules, Adv. Mater. 36 (15) (2024) 2307357, http://dx.doi.org/10.1002/adma.202307357.

[4] PVsyst, Design and simulation software for photovoltaic systems, 2025, https://www.pvsyst.com/. (Accessed 8 March 2025).

[5] D.L. King, W.E. Boyson, J.A. Kratochvil, Photovoltaic Array Performance Model, Tech. Rep., Sandia National Laboratories, 2004, http://dx.doi.org/10.2172/919131.

[6] D. Faiman, Assessing the outdoor operating temperature of photovoltaic modules, Prog. Photovolt., Res. Appl. 16 (4) (2008) 307–315, http://dx.doi.org/10.1002/pip.813.

[7] Sandia National Laboratories, PVsyst cell temperature model, 2025, https://pvpmc.sandia.gov/modeling-guide/2-dc-module-iv/cell-temperature/pvsyst-cell-temperature-model/. (Accessed 8 March 2025).

[8] M. Mattei, G. Notton, C. Cristofari, M. Muselli, P. Poggi, Calculation of the polycrystalline PV module temperature using a simple method of energy balance, Renew. Energy 31 (4) (2006) 553–567, http://dx.doi.org/10.1016/j.renene.2005.03.010.

[9] E. Skoplaki, A. Boudouvis, J. Palyvos, A simple correlation for the operating temperature of photovoltaic modules of arbitrary mounting, Sol. Energy Mater. Sol. Cells 92 (11) (2008) 1393–1402, http://dx.doi.org/10.1016/j.solmat.2008.05.016.

[10] E. Skoplaki, J. Palyvos, Operating temperature of photovoltaic modules: A survey of pertinent correlations, Renew. Energy 34 (1) (2009) 23–29, http://dx.doi.org/10.1016/j.renene.2008.04.009.

[11] T. Townsend, A Method for Estimating the Long-Term Performance of Direct-Coupled Photovoltaic Systems (Master's thesis), University of Wisconsin-Madison, 1989.

[12] M.A. Green, General temperature dependence of solar cell performance and implications for device modelling, Prog. Photovolt., Res. Appl. 11 (5) 333–340, http://dx.doi.org/10.1002/pip.496.

[13] E. Skoplaki, J. Palyvos, On the temperature dependence of photovoltaic module electrical performance: A review of efficiency/power correlations, Sol. Energy 83 (5) (2009) 614–624, http://dx.doi.org/10.1016/j.solener.2008.10.008.

[14] J. Qian, A.F. Thomson, Y. Wu, K.J. Weber, A.W. Blakers, Impact of perovskite/silicon tandem module design on hot-spot temperature, ACS Appl. Energy Mater. 1 (7) (2018) 3025–3029, http://dx.doi.org/10.1021/acsaem.8b00480.

[15] H. Zheng, G. Liu, C. Zhang, L. Zhu, A. Alsaedi, T. Hayat, X. Pan, S. Dai, The influence of perovskite layer and hole transport material on the temperature stability about perovskite solar cells, Sol. Energy 159 (2018) 914–919, http://dx.doi.org/10.1016/j.solener.2017.09.039.

[16] J.P. Bastos, G. Uytterhoeven, W. Qiu, U.W. Paetzold, D. Cheyns, S. Surana, J. Rivas, M. Jaysankar, W. Song, T. Aernouts, J. Poortmans, R. Gehlhaar, Model for the prediction of the lifetime and energy yield of methyl ammonium lead iodide perovskite solar cells at elevated temperatures, ACS Appl. Mater. Interfaces 11 (18) (2019) 16517–16526, http://dx.doi.org/10.1021/acsami.9b00923.

[17] J. Kim, N. Park, J.S. Yun, S. Huang, M.A. Green, A.W. Ho-Baillie, An effective method of predicting perovskite solar cell lifetime–Case study on planar CH3NH3PbI3 and HC(NH2)2PbI3 perovskite solar cells and hole transfer materials of spiro-OMeTAD and PTAA, Sol. Energy Mater. Sol. Cells 162 (2017) 41–46, http://dx.doi.org/10.1016/j.solmat.2016.12.043.

[18] S. Armstrong, W. Hurley, A thermal model for photovoltaic panels under varying atmospheric conditions, Appl. Therm. Eng. 30 (11) (2010) 1488–1495, http://dx.doi.org/10.1016/j.applthermaleng.2010.03.012.

[19] J. Zhou, Q. Yi, Y. Wang, Z. Ye, Temperature distribution of photovoltaic module based on finite element simulation, Sol. Energy 111 (2015) 97–103, http://dx.doi.org/10.1016/j.solener.2014.10.040.

[20] A. Kamppinen, H. Palonen, K. Miettunen, Self-heating of planar perovskite solar cells depending on active material properties, ACS Appl. Energy Mater. 7 (10) (2024) 4324–4334, http://dx.doi.org/10.1021/acsaem.4c00077.

[21] M. Akhsassi, A. El Fathi, N. Erraissi, N. Aarich, A. Bennouna, M. Raoufi, A. Outzourhit, Experimental investigation and modeling of the thermal behavior of a solar PV module, Sol. Energy Mater. Sol. Cells 180 (2018) 271–279, http://dx.doi.org/10.1016/j.solmat.2017.06.052.

[22] M. Usama Siddiqui, A. Arif, L. Kelley, S. Dubowsky, Three-dimensional thermal modeling of a photovoltaic module under varying conditions, Sol. Energy 86 (9) (2012) 2620–2631, http://dx.doi.org/10.1016/j.solener.2012.05.034.

[23] Y. Du, W. Tao, Y. Liu, J. Jiang, H. Huang, Heat transfer modeling and temperature experiments of crystalline silicon photovoltaic modules, Sol. Energy 146 (2017) 257–263, http://dx.doi.org/10.1016/j.solener.2017.02.049.

[24] A. Jones, C. Underwood, A thermal model for photovoltaic systems, Sol. Energy 70 (4) (2001) 349–359, http://dx.doi.org/10.1016/S0038-092X(00)00149-3.

[25] D.L. King, Photovoltaic module and array performance characterization methods for all system operating conditions, in: Proceedings of the NREL/SNL Photovoltaic Program Review Meeting, 1997, pp. 1–22.

[26] S. Tselepis, Y. Tripanagnostopoulos, Economic analysis of hybrid photovoltaic/thermal solar systems and comparison with standard PV modules, 2002.

[27] J.D. Mondol, Y.G. Yohanis, B. Norton, Comparison of measured and predicted long term performance of grid a connected photovoltaic system, Energy Convers. Manage. 48 (4) (2007) 1065–1080, http://dx.doi.org/10.1016/j.enconman.2006.10.021.

[28] A. Muzathik, Photovoltaic modules operating temperature estimation using a simple correlation, Int. J. Energy Eng. 4 (2014) 151–158.

[29] P. Mora Segado, J. Carretero, M. Sidrach-de Cardona, Models to predict the operating temperature of different photovoltaic modules in outdoor conditions, Prog. Photovolt., Res. Appl. 23 (10) 1267–1282, http://dx.doi.org/10.1002/pip.2549.

[30] W. Charles Lawrence Kamuyu, J.R. Lim, C.S. Won, H.K. Ahn, Prediction model of photovoltaic module temperature for power performance of floating PVs, Energies 11 (2) (2018) http://dx.doi.org/10.3390/en11020447.

[31] M. Koehl, M. Heck, S. Wiesmeier, J. Wirth, Modeling of the nominal operating cell temperature based on outdoor weathering, Sol. Energy Mater. Sol. Cells 95 (7) (2011) 1638–1646, http://dx.doi.org/10.1016/j.solmat.2011.01.020.

[32] S. Zandi, P. Saxena, N.E. Gorji, Numerical simulation of heat distribution in RGO-contacted perovskite solar cells using COMSOL, Sol. Energy 197 (2020) 105–110, http://dx.doi.org/10.1016/j.solener.2019.12.050.
[33] P. Saxena, N.E. Gorji, COMSOL simulation of heat distribution in perovskite solar cells: Coupled optical–electrical–thermal 3-D analysis, IEEE J. Photovoltaics 9 (6) (2019) 1693–1698, http://dx.doi.org/10.1109/JPHOTOV.2019.2940886.
[34] Y.F. Makableh, I. Abu Awad, W. Hassan, G. Aljaiuossi, Enhancement of the thermal properties of heterojunction perovskite solar cells by nanostructured contacts design, Sol. Energy 202 (2020) 204–209, http://dx.doi.org/10.1016/j.solener.2020.04.002.
[35] P. Lopez-Varo, M. Amara, S. Cacovich, A. Julien, A. Yaïche, M. Jouhari, J. Rousset, P. Schulz, J.-F. Guillemoles, J.-B. Puel, Dynamic temperature effects in perovskite solar cells and energy yield, Sustain. Energy Fuels 5 (2021) 5523–5534, http://dx.doi.org/10.1039/D1SE01381E.
[36] R. Gehlhaar, T. Merckx, W. Qiu, T. Aernouts, Outdoor measurement and modeling of perovskite module temperatures, Glob. Challenges 2 (7) (2018) 1800008, http://dx.doi.org/10.1002/gch2.201800008.
[37] S. Khanna, S. Sundaram, K. Reddy, T.K. Mallick, Performance analysis of perovskite and dye-sensitized solar cells under varying operating conditions and comparison with monocrystalline silicon cell, Appl. Therm. Eng. 127 (2017) 559–565, http://dx.doi.org/10.1016/j.applthermaleng.2017.08.030.
[38] J. Varjopuro, A. Kamppinen, Comparison of PVK and Si panel temperatures, [Open-source code], 2025, https://github.com/juliavarjop/Comparison_of_PVK_and_Si_panel_temperatures.
[39] G. Notton, C. Cristofari, M. Mattei, P. Poggi, Modelling of a double-glass photovoltaic module using finite differences, Appl. Therm. Eng. 25 (17) (2005) 2854–2877, http://dx.doi.org/10.1016/j.applthermaleng.2005.02.008.
[40] COMSOL, Heat Transfer Module User's Guide, https://doc.comsol.com/6.2/doc/com.comsol.help.heat/HeatTransferModuleUsersGuide.pdf. (Accessed 8 March 2025).
[41] J. Watmuff, W. Charters, D. Proctor, Solar and wind induced external coefficients - Solar collectors, Coop. Mediterr. Pour L' Energ. Sol. 1 (1977) 56.
[42] Y. Lee, A.A. Tay, Finite element thermal analysis of a solar photovoltaic module, Energy Procedia 15 (2012) 413–420, http://dx.doi.org/10.1016/j.egypro.2012.02.050, international Conference on Materials for Advanced Technologies 2011, Symposium O.
[43] W. Hu, X. Li, J. Wang, Z. Tian, B. Zhou, J. Wu, R. Li, W. Li, N. Ma, J. Kang, Y. Wang, J. Tian, J. Dai, Experimental research on the convective heat transfer coefficient of photovoltaic panel, Renew. Energy 185 (2022) 820–826, http://dx.doi.org/10.1016/j.renene.2021.12.090.
[44] S. Sharples, P. Charlesworth, Full-scale measurements of wind-induced convective heat transfer from a roof-mounted flat plate solar collector, Sol. Energy 62 (2) (1998) 69–77, http://dx.doi.org/10.1016/S0038-092X(97)00119-9.
[45] R. Santbergen, J. Goud, M. Zeman, J. van Roosmalen, R. van Zolingen, The AM1.5 absorption factor of thin-film solar cells, Sol. Energy Mater. Sol. Cells 94 (5) (2010) 715–723, http://dx.doi.org/10.1016/j.solmat.2009.12.010.
[46] L.C. Hirst, N.J. Ekins-Daukes, Fundamental losses in solar cells, Prog. Photovolt., Res. Appl. 19 (3) 286–293, http://dx.doi.org/10.1002/pip.1024.
[47] Y. An, T. Ma, X. Li, Energy tracing of photovoltaic cells, Sol. RRL 5 (7) 2100199, http://dx.doi.org/10.1002/solr.202100199.
[48] M.A. Green, Intrinsic concentration, effective densities of states, and effective mass in silicon, J. Appl. Phys. 67 (6) (1990) 2944–2954, http://dx.doi.org/10.1063/1.345414.
[49] S. Singh, C. Li, F. Panzer, K.L. Narasimhan, A. Graeser, T.P. Gujar, A. Köhler, M. Thelakkat, S. Huettner, D. Kabra, Effect of Thermal and structural disorder on the electronic structure of hybrid perovskite semiconductor CH3NH3PbI3, J. Phys. Chem. Lett. 7 (15) (2016) 3014–3021, http://dx.doi.org/10.1021/acs.jpclett.6b01207.
[50] I. Subedi, T.J. Silverman, M.G. Deceglie, N.J. Podraza, PERC silicon PV infrared to ultraviolet optical model, Sol. Energy Mater. Sol. Cells 215 (2020) 110655, http://dx.doi.org/10.1016/j.solmat.2020.110655.
[51] J.M. Ball, S.D. Stranks, M.T. Hörantner, S. Hüttner, W. Zhang, E.J.W. Crossland, I. Ramirez, M. Riede, M.B. Johnston, R.H. Friend, H.J. Snaith, Optical properties and limiting photocurrent of thin-film perovskite solar cells, Energy Env. Sci. 8 (2015) 602–609, http://dx.doi.org/10.1039/C4EE03224A.
[52] W. Shockley, H.J. Queisser, Detailed balance limit of efficiency of p–n junction solar cells, J. Appl. Phys. 32 (3) (1961) 510–519.
[53] M.A. Green, Solar Cells: Operating Principles, Technology, and System Applications, Prentice-Hall, Englewood Cliffs, NJ, USA, 1982.
[54] K. Emery, J. Burdick, Y. Caiyem, D. Dunlavy, H. Field, B. Kroposki, T. Moriarty, L. Ottoson, S. Rummel, T. Strand, M. Wanlass, Temperature dependence of photovoltaic cells, modules and systems, in: Conference Record of the Twenty Fifth IEEE Photovoltaic Specialists Conference-1996, IEEE, 1996, pp. 1275–1278.
[55] N. Reich, W. van Sark, E. Alsema, R. Lof, R. Schropp, W. Sinke, W. Turkenburg, Crystalline silicon cell performance at low light intensities, Sol. Energy Mater. Sol. Cells 93 (9) (2009) 1471–1481, http://dx.doi.org/10.1016/j.solmat.2009.03.018.
[56] C. Berthod, R. Strandberg, G.H. Yordanov, H.G. Beyer, J.O. Odden, On the variability of the temperature coefficients of mc-si solar cells with irradiance, Energy Procedia 92 (2016) 2–9, http://dx.doi.org/10.1016/j.egypro.2016.07.002, Proceedings of the 6th International Conference on Crystalline Silicon Photovoltaics (SiliconPV 2016).
[57] F. Muhammadsharif, S. Hashim, A simple and efficient determination of the ideality factor of solar cells and modules from the knee point of the shunt resistance curve, Arab. J. Sci. Eng. 48 (2023) 8217–8225, http://dx.doi.org/10.1007/s13369-023-07860-3.
[58] J. Haschke, J.P. Seif, Y. Riesen, A. Tomasi, J. Cattin, L. Tous, P. Choulat, M. Aleman, E. Cornagliotti, A. Uruena, R. Russell, F. Duerinckx, J. Champliaud, J. Levrat, A.A. Abdallah, B. Aïssa, N. Tabet, N. Wyrsch, M. Despeisse, J. Szlufcik, S. De Wolf, C. Ballif, The impact of silicon solar cell architecture and cell interconnection on energy yield in hot & sunny climates, Energy Env. Sci. 10 (2017) 1196–1206, http://dx.doi.org/10.1039/C7EE00286F.
[59] W. Zhang, L. He, Y. Meng, H. Kanda, D. Tang, B. Ding, Y. Ding, M.K. Nazeeruddin, X. Li, Dual-site synergistic passivation for highly efficient and stable perovskite solar cells, Adv. Energy Mater. 12 (46) (2022) 2202189, http://dx.doi.org/10.1002/aenm.202202189.
[60] M. Jošt, B. Lipovšek, B. Glažar, A. Al-Ashouri, K. Brecl, G. Matič, A. Magomedov, V. Getautis, M. Topič, S. Albrecht, Perovskite solar cells go outdoors: Field testing and temperature effects on energy yield, Adv. Energy Mater. 10 (25) (2020) 2000454, http://dx.doi.org/10.1002/aenm.202000454.
[61] J.A. Karhu, A.V. Lindfors, W. Wandji Nyamsi, T. Salola, A. Poikonen, M. Pitkänen, T. Mielonen, O. Mantikka, Outdoor Solar Power Laboratories at the Finnish Meteorological Institute, Submitted for publication.
[62] H. Böök, A. Poikonen, A. Aarva, T. Mielonen, M.R. Pitkänen, A.V. Lindfors, Photovoltaic system modeling: A validation study at high latitudes with implementation of a novel DNI quality control method, Sol. Energy 204 (2020) 316–329, http://dx.doi.org/10.1016/j.solener.2020.04.068.
[63] J.-H. Bae, D.-Y. Kim, J.-W. Shin, S.-E. Lee, K.-C. Kim, Analysis on the features of NOCT and NMOT tests with photovoltaic module, IEEE Access 8 (2020) 151546–151554, http://dx.doi.org/10.1109/ACCESS.2020.3017372.
[64] W. Herrmann, C. Monokroussos, K. Lee, Comparison of different approaches to determine the Nominal PV Module Operating Temperature (NMOT), in: 38th European Photovoltaic Solar Energy Conference and Exhibition, 2021.
[65] International Electrotechnical Commission, et al., IEC 61724-1: 2021 Photovoltaic System Performance, Part 1: Monitoring, Tech. Rep., International Electrotechnical Commission, 2021.
[66] L. Karttunen, S. Jouttijärvi, A. Poskela, H. Palonen, H. Huerta, M. Todorović, S. Ranta, K. Miettunen, Comparing methods for the long-term performance assessment of bifacial photovoltaic modules in nordic conditions, Renew. Energy 219 (2023) 119473, http://dx.doi.org/10.1016/j.renene.2023.119473.
[67] J. Kurnik, M. Jankovec, K. Brecl, M. Topic, Outdoor testing of PV module temperature and performance under different mounting and operational conditions, Sol. Energy Mater. Sol. Cells 95 (1) (2011) 373–376, http://dx.doi.org/10.1016/j.solmat.2010.04.022, 19th International Photovoltaic Science and Engineering Conference and Exhibition (PVSEC-19) Jeju, Korea, 9-13 2009.